Science Advances
AAAS

advances.sciencemag.org/cgi/content/full/6/6/eaay6407/DC1

Supplementary Materials for

High mobility in a van der Waals layered antiferromagnetic metal

Shiming Lei, Jingjing Lin, Yanyu Jia, Mason Gray, Andreas Topp, Gelareh Farahi, Sebastian Klemenz, Tong Gao, Fanny Rodolakis, Jessica L. McChesney, Christian R. Ast, Ali Yazdani, Kenneth S. Burch, Sanfeng Wu, Nai Phuan Ong, Leslie M. Schoop*

*Corresponding author. Email: lschoop@princeton.edu

Published 7 February 2020, *Sci. Adv.* **6**, eaay6407 (2020)
DOI: 10.1126/sciadv.aay6407

This PDF file includes:

Section S1. Crystal structure, composition, magnetization, heat capacity, and in-plane resistivity

$GdTe_3$ crystals were characterized by x-ray diffraction (XRD) and SEM/EDX to confirm the structure (fig. S1A) and composition. Right before these characterizations, the crystal surface was cleaned by peeling off the exterior layers with scotch-tape. No impurity phases can be detected in the XRD or SEM/EDX characterizations.

A Curie-Weiss fit to the DC magnetic susceptibility (fig. S1B) is performed on a $GdTe_3$ crystal to determine the effective magnetic moment. The measured effective magnetic moment of 7.91 μ_B/Gd agrees very well with the theoretical value (7.94 μ_B/Gd) for Gd^{3+}, thus suggesting that the magnetic moments are localized below the Fermi level. This indicates that the *R*Te slabs are magnetically localized and therefore have an insulating character, while the Te square-net sheets contribute to the metallic nature of $GdTe_3$.

The temperature-dependent zero-field resistivities on two representative $GdTe_3$ crystals (Sample 1 and 2) are shown in figs. S1C, D. The resistivity of Sample 1 was measured up to 400 K to determine the CDW transition temperature (T_{CDW} = 379 K). The *RRR*s of Sample 1 and 2 are determined to be 358 and 511, respectively. A fit to the quadratic temperature-dependency relation, $\rho(T)= \rho(T)+AT^2$, below T_N = 12 K reveals a prefactor A of 0.55 nΩ cm/K^2 and 0.58 nΩ cm/K^2, respectively. These values are only slightly higher than the typical values for transition metals (*56*), but much lower than that of Bi (7.7 nΩ cm/K^2) (*57*), $SrMnBi_2$ (19 nΩ cm/K^2) (*55*), and $YbMnBi_2$ (5.7 nΩ cm/K^2) (*47*). Since A is inversely proportional to the Fermi temperature, the low prefactor A indicates that light carriers are responsible for the metallic conduction (*44*).

Section S2. STM topography and spectroscopy

A Fourier analysis of the measured STM topographic image is used to reveals the CDW wave vector (*58,59*). Figures S2A, B show the Fourier transformed image with a cross-sectional cut to evaluate the CDW vector. The estimated CDW vector is $q_{CDW} \approx 2/7 \times 2\pi/b = 4.15$ nm^{-1}. The STM spectrum (dI/dV curve) shown in fig. S2C is an averaged result over a small area, using a lock-in amplifier with setpoint current and bias of 60 pA and 800 mV respectively, with a modulation bias of 8 mV. The shape of the dI/dV curve is remarkably similar to those from previous measurements on $TbTe_3$ (*58*) and $CeTe_3$ (*59*). Since dI/dV is proportional to the local density of states (DOS), the reduced intensity in the dI/dV curve reflects the partial gap opening of the Fermi surface (FS). Based on the information from the dI/dV curve, the estimated energy width is $2\Delta_{CDW} \approx 420$ mV, and it gives the CDW gap of ~210 mV. This is similar to that observed $TbTe_3$ (*58*), and $CeTe_3$ (*59*). The finite conductance at zero bias results from the nonzero DOS inside the gap.

Section S3. MR and SdH oscillations

The field dependent in-plane resistivity was measured to reveal MR and SdH oscillations. Figures S3A shows a representative MR measured on Sample 3 at various temperatures. It gives rise to a MR of 1,300% under the field of 9 T at 1.9 K. The in-plane resistivity was also measured under various sample tilt angles (θ) at 1.9 K. The extracted θ dependent SdH oscillations are shown in fig. S3B. The frequency of α oscillation nicely follows the factor of $1/\cos\theta$ up to 60°, suggesting a rather 2D morphology, in agreement with the layered crystal structure. As mentioned in the main text, the SdH oscillations on $GdTe_3$ crystals generally show much weaker high-frequency oscillations compared to the dHvA measurements. Figures 3C, D shows the SdH oscillations on Sample 1 (after polynomial background subtraction) in the range

of 6 T to 9 T and its FFT spectrum. The γ_1 frequency that was resolved in the dHvA measurement, was not resolved here, most likely due to its much weaker intensity compared to γ_2. Note that in all samples where SdH oscillations were measured, the third harmonic 3α can be observed. In some samples with slightly lower *RRR* (such as Samples 3 and 4), the higher-frequency oscillations (β, γ, δ and η) cannot be resolved, and the third harmonic 3α oscillation also has a lower intensity. The dominant α oscillation in these samples (Samples 3 and 4) thus allows for an accurate evaluation of the cyclotron effective mass for the α pocket.

Section S4. Comparison of the FS pockets from QO measurements to the calculated ones

According to the Onsager relationship $F = (\Phi_0/2\pi^2)S_F$, where Φ_0 is the magnetic flux quantum and S_F is the cross-sectional area of the FS, the α, β_1, β_2, γ_1 and γ_2 oscillations that were resolved in dHvA measurement correspond to 0.27%, 2.13%, 2.28% 3.67% and 3.82 % of the Brillouin zone (BZ) area, respectively, and the η, δ_1 and δ_2 oscillations that were additionally resolved from SdH measurement are 10.1%, 16.7 % and 17.8 % of BZ area, respectively.

Previously, band-structure calculations were performed for the unmodulated structure of $LaTe_3$ (*30*) and $LuTe_3$ (*60*) using the linear muffin-tin orbital (LMTO) method, and they predicted the existence of two electron-pockets (β and γ) encircling the X point of the BZ (see fig. S6 for a sketched version of the FS). If the CDW modulation is considered, the two pockets around X remain closed, as was suggested by the angle-resolved photoemission spectroscopy (ARPES) measurement on $CeTe_3$ (*61*). Particularly, the band-structure calculations on $LaTe_3$ (*30*) predicted that β has a size of 2.14% - 2.79% (depending on k_z) of the BZ area and γ has a size of 3.68% - 3.82% (depending on k_z) of the BZ area. These predictions match the size of the β and γ pockets observed in the dHvA and SdH oscillations very well. Therefore, the pairing of β_1/β_2 and γ_1/γ_2 pockets are attributed to the "neck" and "belly" extremal orbits of corrugated FS due to the slight

k_z dispersions. Experimentally, the difference in β_1 and β_2 frequencies is smaller than that from calculations. Based on the results from band-structure calculations, the hole-pockets are much larger than the electron-pockets of β and γ. When the CDW modulation is considered, replica bands are formed in superposition to the original bands, and hybridizations of these bands can lead to the formation of new FS pockets, with a reduced size. This scenario was proposed for the explanation of the ARPES resolved FS in $CeTe_3$ (*39*). Considering that γ is the largest electron-pocket predicted in the calculations, we attribute the η and δ pockets to be reconstructed hole-pockets. The small α pocket is also likely the product of FS reconstruction from the CDW.

Section S5. Carrier concentration estimations from QO measurements versus Hall measurements

The carrier concentrations can be estimated from the size of the FS pocket determined by QO measurements. Assuming a strict 2D geometry (no k_z dispersion), the carrier density n_{2D} per monolayer $GdTe_3$ per unit area is given by Luttinger's theorem as

$$n_{2D} = 2\frac{S_F}{(2\pi)^2} = \frac{F}{\Phi_0} \quad \text{(S1)}$$

where S_F is the 2D cross-sectional area of FS, Φ_0 is the magnetic flux quantum and F is the QO frequency. Since we have detected a tiny k_z dispersion, equation (S1) can be slightly modified to consider the k_z dispersion as

$$n_{2D} = \frac{S_{F1}+S_{F2}}{(2\pi)^2} = \frac{F_1+F_2}{2\Phi_0} \quad \text{(S2)}$$

where F_1 and F_2 are the measured frequency pair. The 3D carrier concentration can be estimated taking the number of $GdTe_3$ layers per unit thickness into consideration. In the $GdTe_3$ structure, each monolayer is c = 1.28 nm thick from our XRD measurement on the single crystals. Therefore, the 3D carrier concentration, n_{3D}, is calculated as

$$n_{3D} = \frac{n_{2D}}{c} = \frac{F_1 + F_2}{2\Phi_0 c} \quad \text{(S3)}$$

Using equation (S3), the overall electron carrier concentration is estimated to be 5.0×10^{20} cm^{-3} by considering the combination of β and γ pockets. The hole carrier concentration is estimated to be 2.4×10^{21} cm^{-3} by considering both η *and* δ pockets. Note that α is not considered for the carrier concentration estimation because of its negligible size. Overall, the carrier concentration estimated from the QO frequencies reasonably agrees with those obtained from a two-band model fit to the Hall data. We note that a previous optical conductivity measurement on $GdTe_3$ has suggested that only 3.2% of the original FS remains ungapped after the CDW modulation (*62*). Our current comprehensive QO and Hall measurements thus provide a more accurate description on the FS geometry and carrier concentration.

Section S6. ARPES measurement

Soft x-ray ARPES measurements were performed at 9 K at the IEX beam line (29ID, Advanced Photon Source, Argonne National Laboratory) using a hemispherical Scienta R4000 electron analyzer with a pass energy of 200 eV (energy and angular resolution are 220 meV and 0.1°, respectively). The ARPES spectra were recorded with right circular polarized light at a photon energy of 500 eV. $GdTe_3$ was cleaved cold, 30 K, and then cooled down to 9 K for the ARPES measurements. Figures S6A, B shows the FS geometry at and slightly below the Fermi level, E_F. The Fermi velocity (figs. S6D, E) is estimated from two cross-sectional cuts (Path 1 and 2 in fig. S6C)

Section S7. Air sensitivity study and Raman spectroscopy of $GdTe_3$ thin flakes

The air sensitivity test was performed under ambient condition. While the thin flakes are stable in air for a short while, they start to degrade upon heating above ~100 °C or exposing in air for a

longer time (>1 hours). Heating in inert atmosphere keeps the flakes intact, however (fig. S7). The Raman spectroscopy of exfoliated $GdTe_3$ thin flakes was monitored in an inert atmosphere (fig. S8). As expected for strongly absorbing samples, the Raman signal was strongly enhanced as the material was thinned. For thin flakes down to 15 nm the Raman signal is nearly un-altered, however for thinner samples a strong enhancement and small redshift was observed for a single mode at 125 cm^{-1}. Simultaneously, a mode near 120 cm^{-1}, seems to disappear. The origin for this behavior is currently not clear, but maybe the result of it merging with the intense mode. However, as all other modes remain close to their bulk values, we conclude the structure is intact. We note that the initial polarization and temperature dependent measurements on bulk suggest that the mode at 120 cm^{-1} has the same symmetry and dependence on the CDW as the other modes, further suggesting the structure is largely un-altered by thinning.

Section S8. Additional notes on mobility for materials shown in Table 2

The mobility values that are listed in Table 2 can be classified into four categories: (1) mobilities (μ_q) derived from quantum lifetime from QO measurements, (2) transport mobilities (μ_t) determined from Hall measurement, (3) the transport mobilities from a combination of QO and residual resistivity measurements (denoted as "hybrid"), and (4) magnetoresistance. The mobility values determined from these methods can be different. The mobility derived from quantum lifetime is generally smaller than the transport mobility, as noted in the main text. In the third method (the "hybrid method"), the QO frequencies are used to estimate the carrier concentration, which can be underestimated due to the possible unresolved FS pockets in QO measurements. With further one-carrier assumption ($1/\rho = ne\mu$), it leads to an overestimation of the averaged carrier mobility. The magnetoresistance method is sometimes used to estimate the mobility when the experimental data can be well characterized by a certain theoretical model.

Table S1. An overview of the $GdTe_3$ samples (bulk and thin-flake geometries), on which we have performed transport measurements in this work. Note: The residual resistivity ratio (*RRR*) is defined in the main text as ρ_{xx} (300 K)/ρ_{xx} (2 K) from the in-plane resistivity (ρ_{xx}) measurements under zero magnetic field; the magnetoresistance (MR) is defined as the ratio of the change of ρ_{xx} under magnetic field, $(\rho_{xx}(H) - \rho_{xx}(0))/\rho_{xx}(0) \times 100\%$, where $\rho_{xx}(0)$ is the resistivity at zero-field. The thickness of the bulk samples (Sample 1-5) ranges from ~10 μm to ~30 μm and the thin flake sample 6 and 7 are 22 nm and 19 nm thick, respectively. Although the *RRR* of thin flake sample 7 is not measured due to imperfect contacts during the cooling process, SdH oscillations can be clearly identified at low temperature (fig. S3).

Sample Number	*RRR*	MR (9 T)	Sample Geometry
1	358	1400%	Bulk
2	511	2800%	
3	315	1300%	
4	188	970%	
5	825	2900%	
6	67	650%	Thin flake (22 nm)
7	NA	NA	Thin flake (19 nm)

Table S2. Material properties derived from QO measurements. F, oscillation frequency; m^*, cyclotron effective mass; m_e, free electron mass; T_D, Dingle temperatures; τ_q, quantum lifetime; μ_q, mobility derived from quantum lifetime.

FS Pocket	F (T)	m^*/m_e	T_D (K)	τ_q ($\times 10^{-14}$ s)	μ_q (cm^2/Vs)	Method	Sample Geometry
α	60	NA	NA	NA	NA	dHvA	Bulk
β_1	472	0.174	7.2	16.9	1710		
β_2	506	0.162	9.0	13.5	1464		
γ_1	813	NA	NA	NA	NA		
γ_2	847	0.213	6.9	17.5	1446		
α	61 (59)	0.106 NA	18.9 (10.0)	6.4 (12.1)	1165 (2012)	SdH	Bulk*
β_1	473	NA	NA	NA	NA		
$\beta 2$	511	NA	NA	NA	NA		
γ_2	852	NA	NA	NA	NA		
η	2230	NA	NA	NA	NA		
δ_1	3708	NA	NA	NA	NA		
$\delta 2$	3948	NA	NA	NA	NA		
α_1	37	NA	NA	NA	NA	SdH	Thin flake†
α_2	49	NA	NA	NA	NA		
β_1	398	NA	NA	NA	NA		
β_2	421	NA	NA	NA	NA		
γ_2	839	NA	NA	NA	NA		

*The material parameters for the α pocket are from Sample 3 and Sample 5 (in the parentheses, the same effective mass is assumed). The parameters for other pockets are from Sample 1.
†Material parameters from Sample 7.

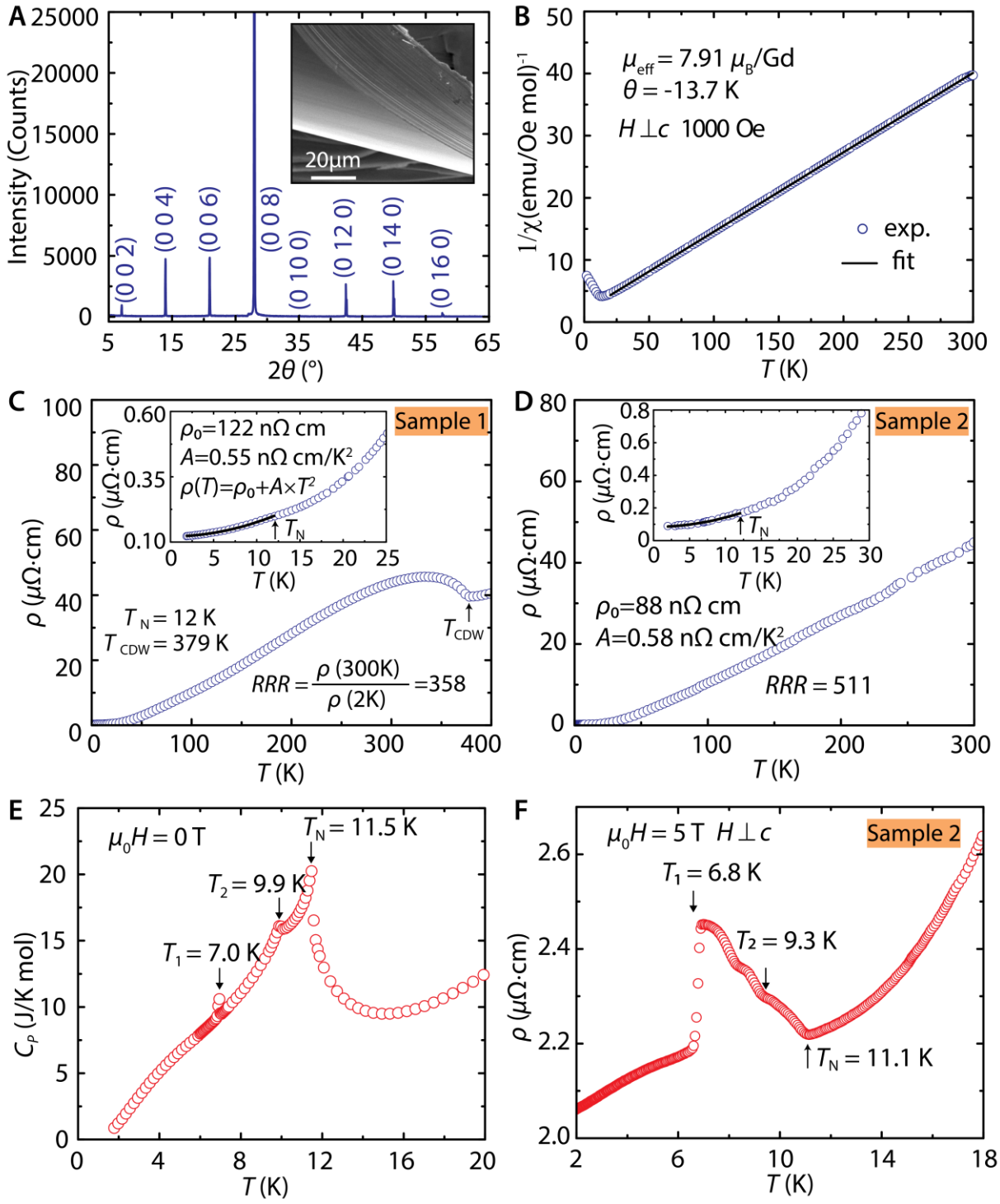

Fig. S1. X-ray diffraction pattern, magnetization, and in-plane resistivity measurements on bulk $GdTe_3$ crystals. (**A**) X-ray diffraction was measured on a plate-like single crystal so that only the (00*l*) diffractions are visible. The inset shows a side-view SEM image, highlighting the

layering morphology of $GdTe_3$ crystals. (**B**) A Curie-Weiss fit to the inverse magnetic susceptibility in the paramagnetic regime. The Weiss temperature , and the effective moment μ_{eff} are determined to be -13.7 K and 7.91 μ_B/Gd, respectively. (**C, D**) Temperature dependent in-plane resistivity of Sample 1 and 2, respectively. Note that the resistivity is measured up to 400 K on Sample 1, and the CDW transition is visible at T_{CDW} = 379 K. The inset shows the low temperature resistivity and its quadratic fit (black line) up to T_N. (**E**) Zero-field heat capacity and (**F**) in-plane resistivity under a 5 T field. T_1, T_2 and T_N correspond to the temperatures of three transitions determined from the DC magnetization measurement (Fig. 1C in the main text). Note that the three transitions appear at slightly lower temperatures in (F) than (E), due to the existence of applied magnetic field.

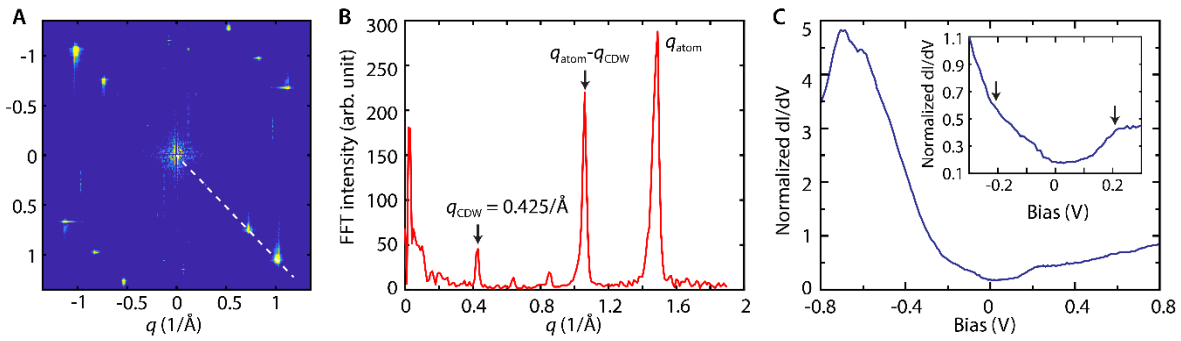

Fig. S2. CDW revealed by STM on a $GdTe_3$ crystal. (**A**) 2D FFT analysis of an STM topography image on a $GdTe_3$ crystal. (**B**) A cross-sectional line-cut (the path is indicated as a dashed line in **A**) of the FFT image. The CDW vector is estimated to be q_{CDW} = 4.25 nm^{-1}. (**C**) dI/dV curve. Inset shows the zoom-in spectrum. The arrows mark the edge location for the estimation of the CDW gap Δ_{CDW}.

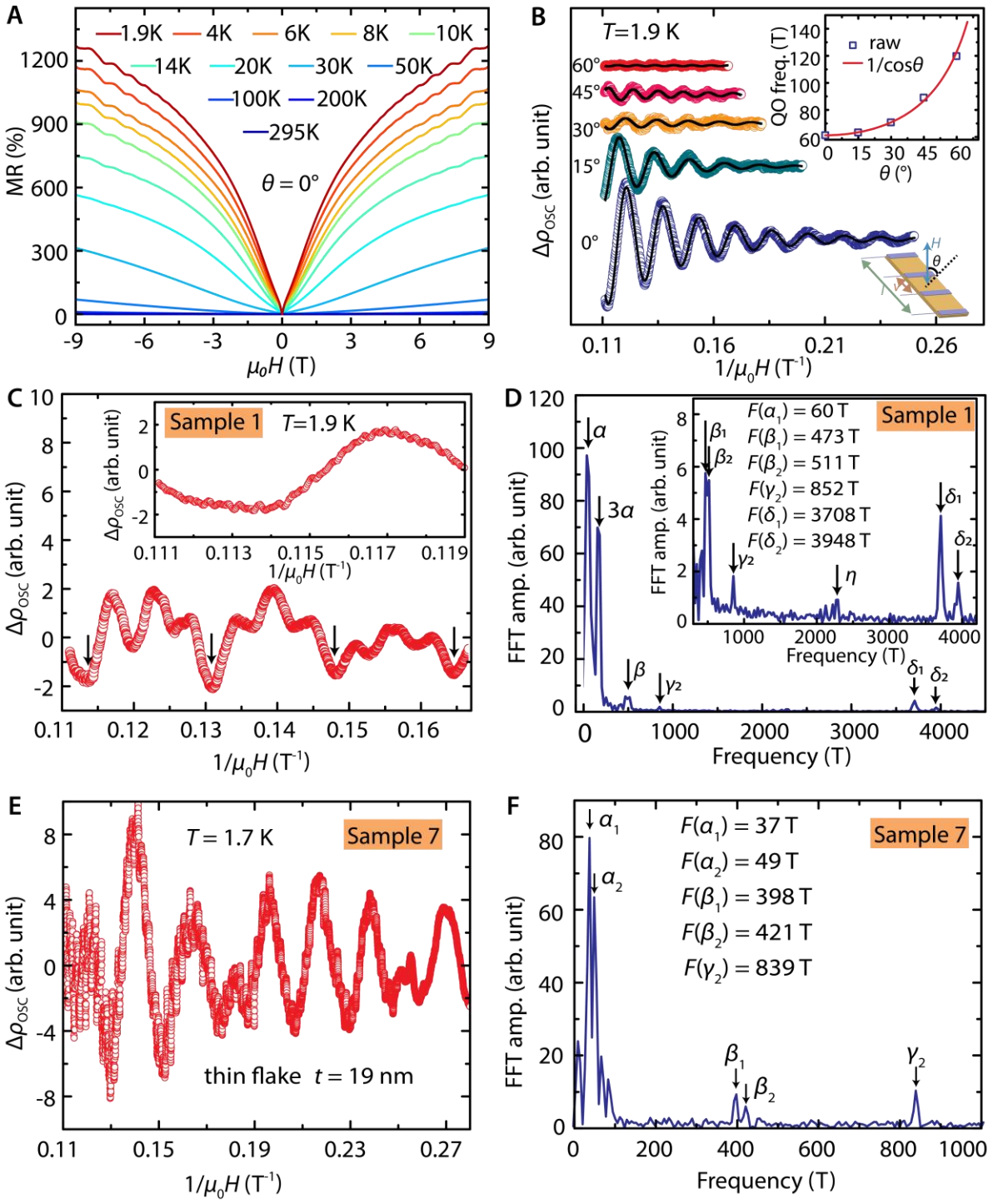

Fig. S3. MR and SdH oscillations. (**A**) MR measured on Sample 3 at various temperatures for the field perpendicular (θ = 0°) to the $GdTe_3$ layering plane. MR = ($\rho_{xx}(H)$ - $\rho_{xx}(0)$)/$\rho_{xx}(0)$ ×

100%, where $\rho_{xx}(0)$ is the in-plane resistivity at zero-field. (**B**) The tilt angle (θ) dependent SdH oscillations, $\Delta\rho_{\mathrm{OSC}}$. $\Delta\rho_{\mathrm{OSC}}$ are extracted from the field dependent in-plane resistivity after a polynomial background subtraction. The top inset shows the derived SdH oscillation frequency as a function of θ. The solid line is a fit assuming an ideal cylindrical Fermi surface geometry. The bottom inset is an illustration of the measurement geometry. The dashed line is normal to the plate-like sample plane. (**C**) SdH oscillations in the range of 6 T to 9 T measured on Sample 1. The inset shows a zoom-in view of the quantum oscillations, revealing the high-frequency oscillations. The arrows indicate the valley of the α oscillation. The third harmonic 3α oscillation is clearly revealed between two neighboring valleys. (**D**) FFT spectrum of the SdH oscillations shown in (C). The inset shows a zoom-in view of the FFT spectrum, revealing the existence FS pockets α, β_1, β_2, γ_2, η, δ_1, δ_2 (the η, δ_1 and δ_2 pockets were not resolved in the dHvA measurements). Note that the η pocket is better resolved in the SdH oscillation extracted between 7 T to 9 T. (**E, F**) SdH oscillations measured on a 19-nm thin flake**.** Note that two α pockets are identified and denoted as α_1 and α_2 in (F). The FFT spectrum of the SdH oscillation appears similar to that shown in (D) on a bulk sample, except that η, δ_1 and δ_2 pockets are not resolved in the 19-nm thin flake. Overall, each resolved FS pocket in the thin flake shows a smaller size than that in the bulk sample.

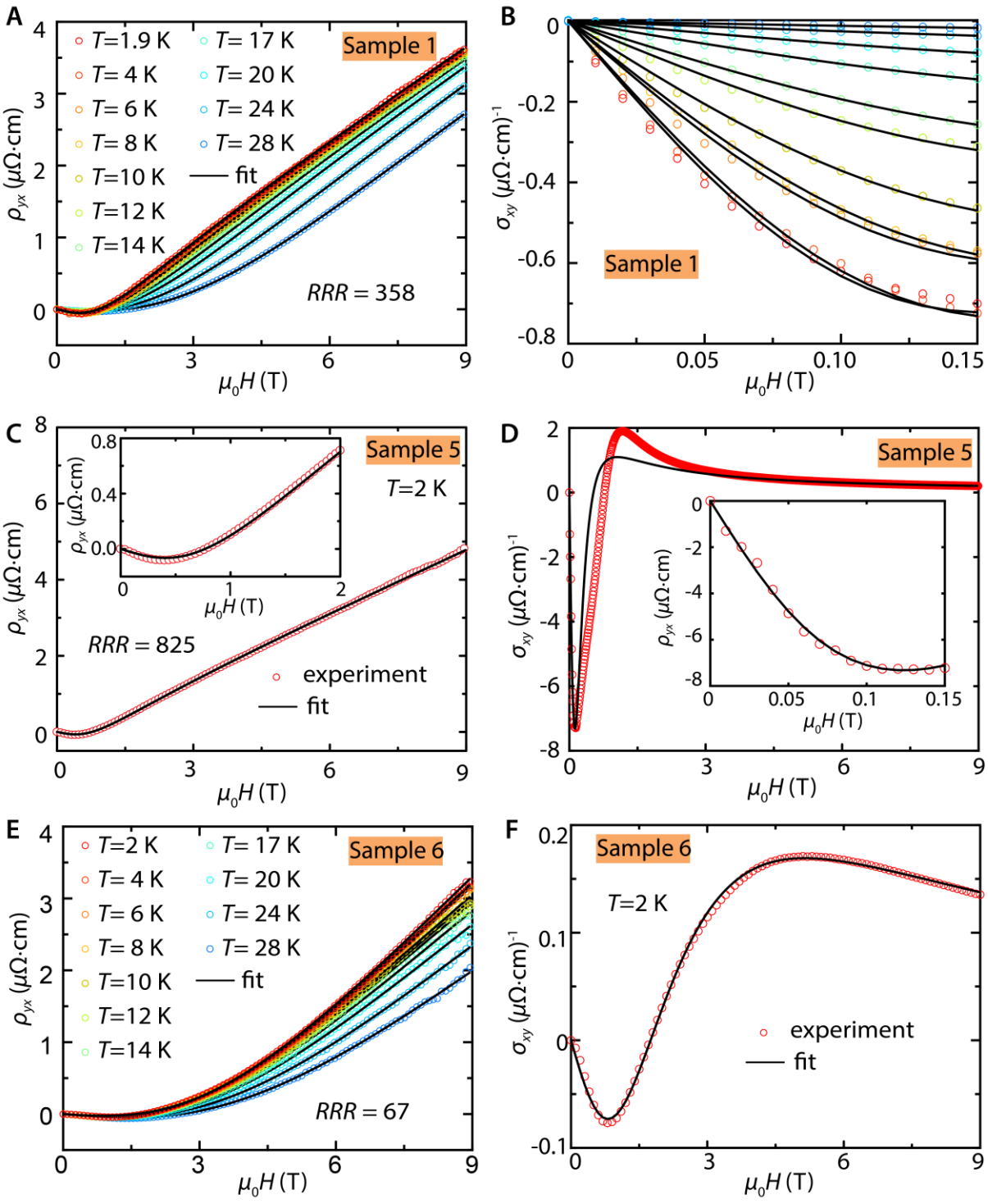

Fig. S4. Two-band model fits to the Hall resistivity and conductivity at various temperatures on multiple samples. (**A, B**) The Hall resistivity and low-field Hall conductivity,

respectively, measured on Sample 1 with their two-band model fits. (**C, D**) The Hall resistivity and Hall conductivity, respectively, measured on Sample 5 with their two-band model fits. Inset shows the low-field region. The fit in (C) results in $n_e = 1.59 \times 10^{21}\,cm^{-3}$, $n_h = 2.74 \times 10^{21}\,cm^{-3}$, $\mu_t(e) = 113{,}000\ cm^2\ V^{-1}\ s^{-1}$ and $\mu_t(h) = 15{,}000\ cm^2\ V^{-1}\ s^{-1}$, while the fit in (D) results in $n_e = 2.28 \times 10^{21}\,cm^{-3}$, $n_h = 3.43 \times 10^{21}\,cm^{-3}$, $\mu_t(e) = 61{,}200\ cm^2\ V^{-1}\ s^{-1}$ and $\mu_t(h) = 23{,}500\ cm^2\ V^{-1}\ s^{-1}$. (**E, F**) Hall resistivity and conductivity, respectively, measured on Sample 6 with two-band model fits.

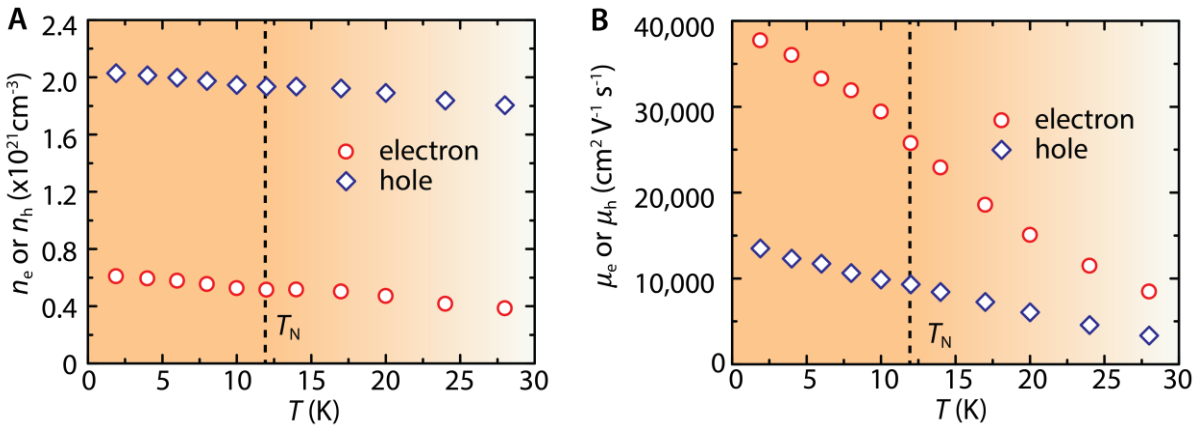

Fig. S5. Temperature-dependent carrier concentrations and mobilities from two-band model fits to the Hall conductivities measured on sample 1.

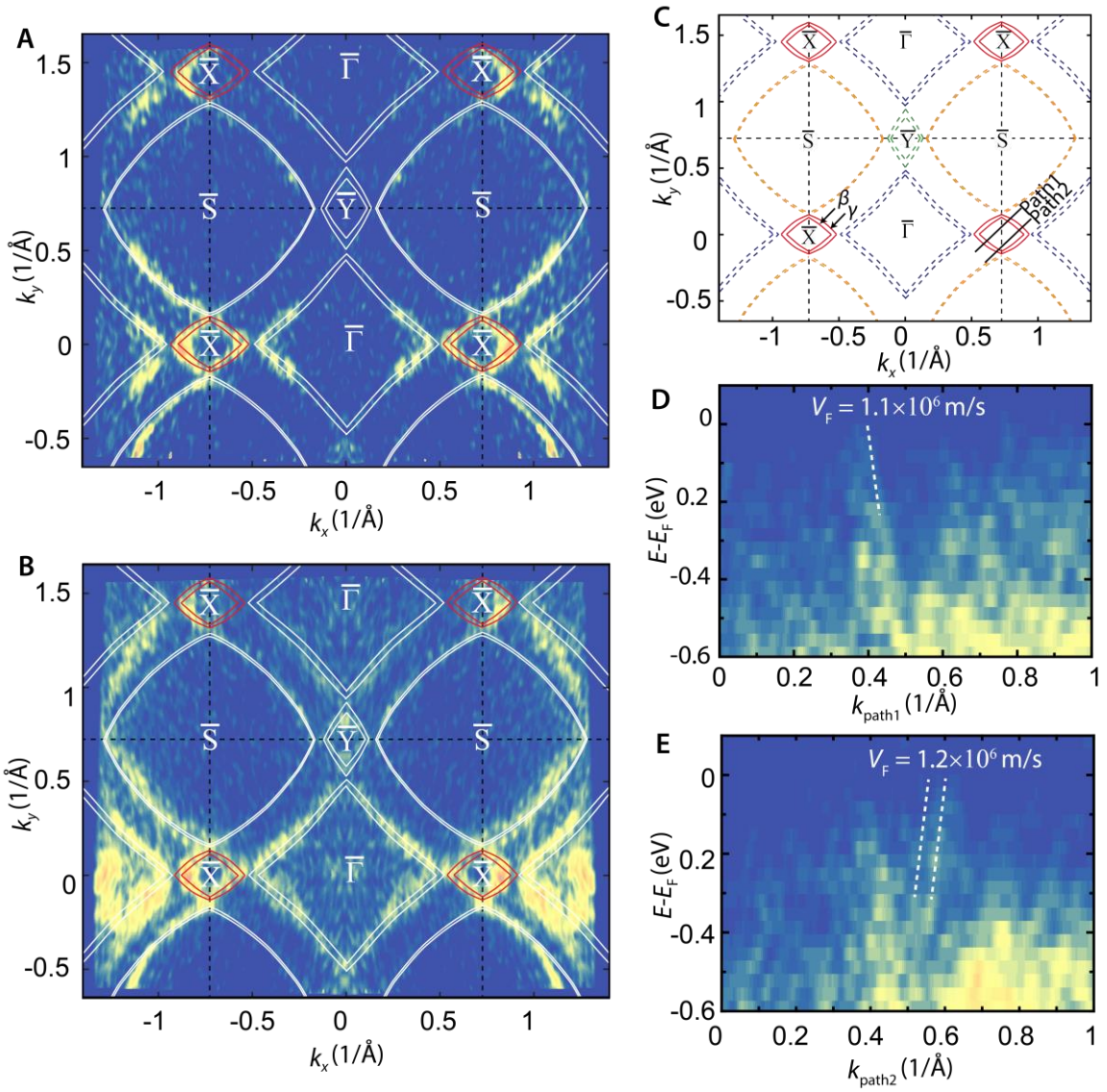

Fig. S6. FS measured by ARPES and gap opening by the CDW in $GdTe_3$. (**A**) FS obtained by integration of the spectral weight in a 50 meV window around E_F. (**B**) The constant energy plots of the spectral weight in a larger window of 130 meV around $E = E_F$-0.18 eV. (**C**) Schematic FS at $k_z = 0$ plane of bulk $GdTe_3$ based on the ARPES results and prior DFT calculations on $LuTe_3$ (*60*). Note that both β and γ pockets (solid lines) around X survive despite the existence of CDW, while the pockets around Γ, S and Y (colored dashed lines) are partially or fully gapped by the CDW. The black dashed lines indicate the BZ boundaries, not considering

the CDW. The two black solid lines indicate the cross-sectional paths for the extraction of Fermi velocity. (**D, E**) Band dispersion along Path 1 and 2 in (C). The dashed lines represent linear fits to the bands near the Fermi level (E_F). The bilayer splitting is visible in (E), as indicated by the two dashed lines. The size of the bilayer splitting is evaluated to be 0.04~0.05 $Å^{-1}$, which corresponds to $0.027a^*$~$0.034a^*$ near $k_y = 0$ at $E = E_F$, where $a^* = 2\pi/a$ (a is sub-unit cell parameter of $GdTe_3$). The value is close to the bilayer splitting ($0.025a^*$) observed in YTe_3 in a previous ARPES experiment (*62*). The size of ARPES resolved β and γ pockets are in reasonably good agreement with those determined by QO measurements. Note: The constant energy plots in (A) and (B) are symmetrized with respect to k_x. The ARPES spectra were recorded with right circular polarized light at a photon energy of 500 eV.

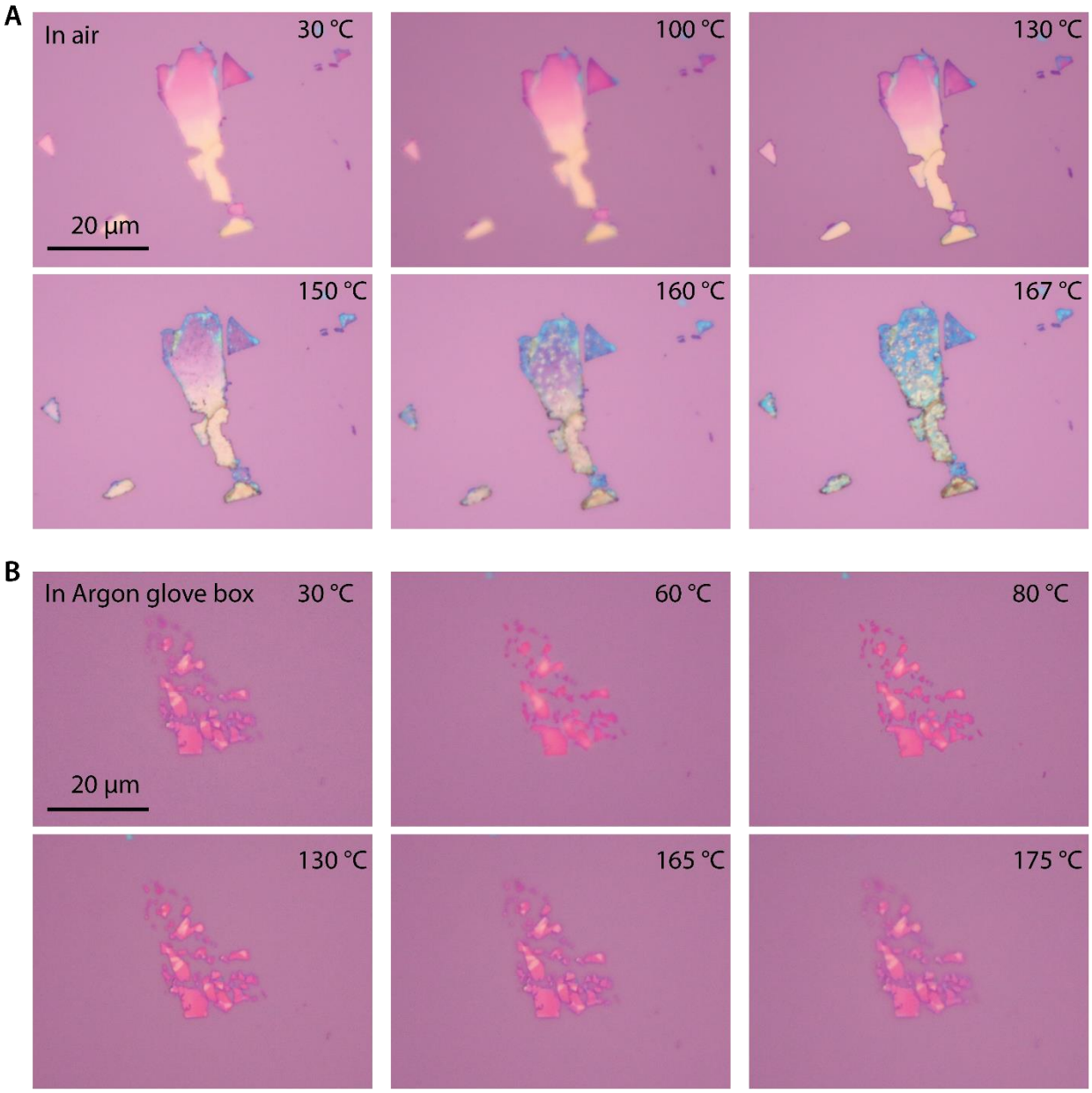

Fig. S7. Air sensitivity of $GdTe_3$ thin flakes. Heat treatment to above ~100 °C in air (**A**) will result in the degradation of thin flakes in a short while, but they remain stable when heated inside the argon-filled glovebox (**B**).

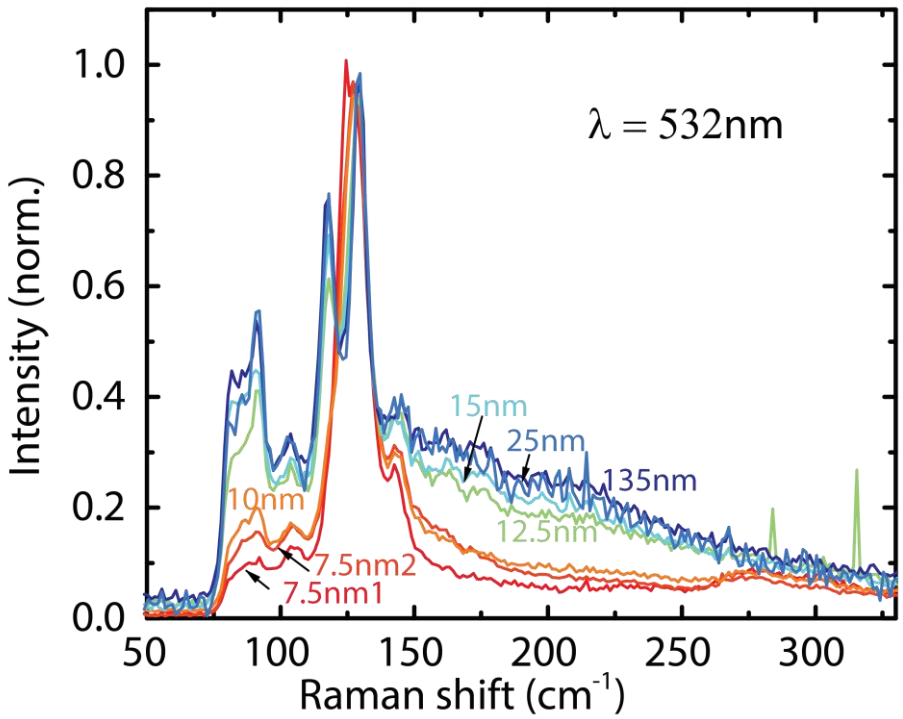

Fig. S8. Raman spectroscopy on a series of $GdTe_3$ thin flakes with varying thicknesses. No major change is observed in the Raman data with thickness. The Raman spectrum on 135 nm thick pieces resembles that of a bulk crystal.